Efficiency Mode Analysis of a Continuous Wave Rotating Magnetic Field Thruster Informed by a Validated Fluid Model

IEPC-2024-761

Presented at the 38th International Electric Propulsion Conference, Toulouse, France
June 23-28, 2024

Grace Zoppi,* Tate M. Gill,† Christopher L. Sercel,‡ and Benjamin A. Jorns§
University of Michigan, Plasmadynamics and Electric Propulsion Laboratory, Ann Arbor, MI, 48109, USA

A computational model for a continuous-wave, Rotating Magnetic Field (RMF) thruster is employed to characterize the dominant efficiency mode losses during operation. The test article is a 10-kW class, conical configuration that employs both an applied magnetic field and three saddle-shaped coil antennas to produce a time-dependent RMF. The computational framework is a quasi-1D formulation based on equations for neutral and ion continuity, ion momentum, and electron temperature. Key free parameters in the model include a factor for magnetic wall confinement, the contribution of a self-induced magnetic field to the RMF, an anomalous collision frequency, and the plume divergence angle. The free parameters are inferred by regressing the model's prediction for thrust and power coupled into the plasma against experimental measurements of the test-article. These measurements were taken over a range of operating conditions with an applied magnetic field of 77-135 G and plasma-coupled power of 5.6-7.1 kW for a constant RMF frequency and flow rate. Efficiency and constituent power modes of the thruster are extracted from the calibrated model. The dominant loss process is the residual thermal energy at the thruster's exit plane, accounting for $\sim 45-55\%$ of the total power coupled to the plasma. The calibrated model was then leveraged to identify possible design strategies to improve performance. These results show that increasing the magnitudes of the applied radial and rotating magnetic field serves as the prime factor to improve overall thruster efficiency.

I. Introduction

The Rotating Magnetic Field (RMF) thruster, an inductive electric propulsion (EP) device, offers key advantages over other state-of-the-art EP technologies. While more mature technologies like Hall Effect Thrusters and Gridded Ion Thrusters now serve the propulsion needs for several commercial and governmental missions, such as station keeping, LEO to GEO transfers, and interplanetary robotic missions, there are notable challenges in extending these technologies to certain new mission architectures of strategic interest. For example, while state-of-the-art electric propulsion classically resides in the 1-5kW range,[1] there is a growing need for thrusters that operate in a higher-power regime for applications such as a crewed mission to Mars.[2] Conventional EP technologies have difficulties with size and mass when scaling to the power level necessary to facilitate these high-power missions. Similarly, while noble gases such as xenon, krypton, and argon have been predominately used as the propellant of choice for EP systems, there is growing interest in the use of non-conventional propellants to facilitate processes such as in-situ resource utilization, multi-mode propulsion, and air-breathing propulsion. These applications present the unique challenge that some of the alternative propellants of interest can poison the thermionic cathodes necessary to operate conventional EP systems.[3–6] Because of these hurdles and the desire to extend the operating envelope of conventional technologies, there is a need to explore alternative thruster architectures.

*PhD Candidate, Aerospace Engineering, gzoppi@umich.edu.
†Assistant Research Scientist, Aerospace Engineering, tategill@umich.edu.
‡Postdoctoral Fellow, Aerospace Engineering, csercel@umich.edu.
§Associate Professor, Aerospace Engineering, bjorns@umich.edu.

Inductively-coupled plasma thrusters (IPTs) are a potentially promising architecture that, in principle, can operate on alternative propellants and scale favorably to high-power applications. IPTs operate on Faraday's law, where a time-varying current inductively produces a Lorentz force to accelerate its propellant. This process does not require plasma wetted electrodes, as energy is coupled wirelessly into the plasma. Additionally, the energy coupling mechanism has comparatively high thrust-densities relative to electrostatic schemes such as Hall or Gridded Ion Thrusters.[7] With that said, there are challenges that have precluded IPTs from wide-spread adoption. Chief among these is the need for very high transient voltages and currents in the driving circuit to facilitate effective inductive coupling. This can be problematic for the power processing unit and the lifetime of the thruster.[8]

The rotating magnetic field (RMF) thruster, a design variation on IPTs, can circumvent these traditional obstacles while maintaining their key advantages. In the RMF thruster, the current induced in the plasma is generated by a rotating magnetic field such that the resulting Lorentz force depends on the frequency of rotation rather than the magnitude of applied currents in the driving circuit. This, in principle, reduces the need for large voltages and currents to generate thrust.[9]

In light of these advantages, several groups have constructed and characterized the performance of RMF test articles over the past two decades. The majority of these studies were conducted using pulsed operation i.e. where the RMF was applied using a limited duty cycle.[10–14] Although these previous works have yielded new insights into the operation of these devices, the maximum peak efficiency of this class of device to date has been low compared to other technologies. The highest value reported has been $\sim 8\%$,[10] though this efficiency measurement is likely an overprediction given that the calculation did not take into account full power supply losses, plume divergence, or mass utilization.[9]

In an effort to identify the mechanisms driving this low performance, subsequent parametric experimental studies conducted at the University of Michigan (UM) identified radiative losses as the main factor, contributing to $\sim 80\%$ of the total power loss in a pulsed operation mode.[15] To mitigate this issue caused by high ion densities in the thruster, an updated iteration of the RMF test article was developed to operate in continuous-wave (CW) operation. The hypothesis was that a non-pulsed mode would allow for lower densities in the thruster at a given power, thereby reducing radiative losses. Subsequent testing performed at UM did ultimately show the efficiency of the thruster was increased from 0.5% to 2.9% when operating in a CW mode.[16]

While this increase in efficiency demonstrated that CW operation is a promising operational path for the RMF thruster, the performance is still an order of magnitude lower than state-of-the-art electric propulsion systems. In an effort to further improve performance in this mode, there is a need to identify and potentially mitigate the driving detractors to performance. In practice, however, experimental techniques for characterizing the efficiency modes (divergence, mass utilization, etc.) of this class of thruster are inherently time consuming, intensive, and perturbative. On the other hand, computational models validated against experimental data that is more easily collected, such as performance, can offer an expedient alternative tool for assessing possible efficiency modes. This type of tool, once validated, also could in practice enable a preliminary assessment of design improvements. With this objective in mind, the goal of this work is to develop and calibrate a reduced fidelity model of a continuous wave RMF thruster, to interpret its results to illustrate the key factors that reduce performance, and to leverage the model to identify design strategies to reduce these losses.

To that end, this paper is structured in the following way. We start by laying out the RMF operating principles and the key assumptions made for simplifying the system into a set of quasi-1D equations. Next, we present the details of the quasi-1D computational framework and experimental test campaign utilized to calibrate the model. Following this, we describe the efficiency modes and the contribution of the inelastic process to the total plasma-coupled power, as predicted by the model. The results lend credence to the model's validity. Finally, we use the model to establish scaling trends for a future RMF test article by conducting three trade studies and an overall model-driven design optimization.

II. RMF Principle of Operation

Fig 1a illustrates the canonical geometry for the type of RMF thruster we investigated in this study. This test article consists of an open tapered cone that bounds a plasma discharge. Saddle shaped antenna pairs (typically 2-3 pairs) surround this cone with their common axes intersecting the centerline of the thruster. Concentric solenoids, which produce the applied magnetic field, encapsulate the antenna and cone structure.

An ionization source, typically a hollow cathode, provides a seed plasma for igniting the discharge.

As shown in Fig 1b-1d, during operation, the solenoids apply a steady magnetic field with a radial gradient while the seed plasma is injected into the thruster. Neutral gas, in turn, can be flowed into the geometry from both an upstream and downstream diffuser depending on the desired configuration. The antennas then fire sequentially in such a way to generate a rotating magnetic field around the central axis of the thruster. The frequency of this rotation is tailored so that it exceeds the ion cyclotron frequency but is less than the electron cyclotron frequency in order to only effect the electron motion. The rotation of the magnetic field, per Faraday's law of induction, results in a time-varying axial electric field. The interaction between this axial electric field and the RMF drives an azimuthal electron current via a Lorentz force. The resulting strong electron drift facilitates additional impact ionization of the inflowing gas, generating a higher density plasma and thereby further increasing the electron current. A subsequent Lorentz force interaction between the azimuthal electron current and the radial magnetic field, supplied from the solenoids, accelerates electrons out of the thruster. Since the ions from the discharge remained unmagnetized (by virtue of the frequency of the RMF), their acceleration is driven by the ambipolar electric field that results from the escaping electrons.

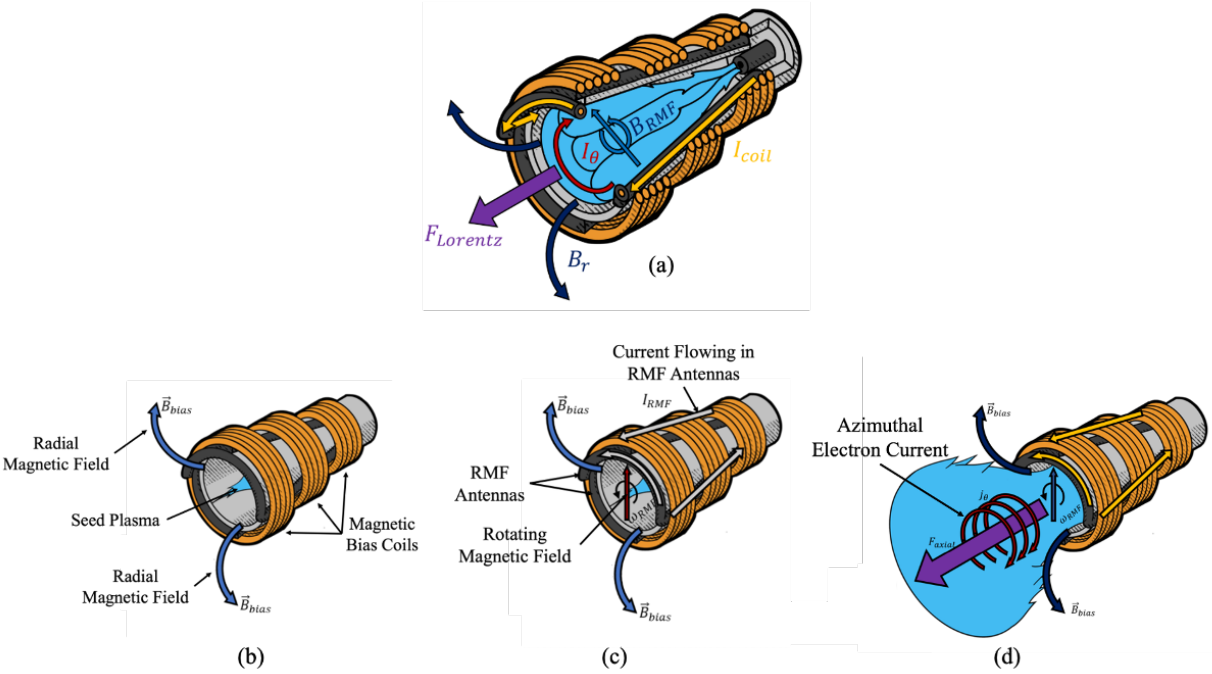

Figure 1: (a) Sectional view of an RMF thruster and the internal processes that result in thrust generation.[17] (b) A steady magnetic field with a radial gradient is applied as seed plasma is injected into the thruster chamber. (c) The antennas fire sequentially to create an RMF as electrons are entrained and more particles are ionized. (d) An azimuthal current is created, and ions are accelerated via the Lorentz force. Reproduced from Ref. [15].

III. Quasi 1D Model Development

Informed by the qualitative description for the principle of operation in the preceding section, we describe here our approach to modeling this process. To this end, we first overview how the domain is simplified and discretized. We then introduce the governing equations for the thruster operation. Finally, we review the quasi-1D numerical techniques utilized to implement the model.

A. Model Domain Discretization

In order to model the RMF thruster, we simplify the system to a quasi-1D axial domain with a conically increasing cross sectional area. Fig 2 illustrates this discretization, in which each subsequent cylindrical cell in the domain is defined by an increasing cell-averaged radius. The dimensions of each cell are predicated upon the thruster's total length, the thruster's half-angle, and the number of cells desired. The incremental axial distance, dz, is used to determine the cell's central z-coordinate along with the associated radius of each cell.

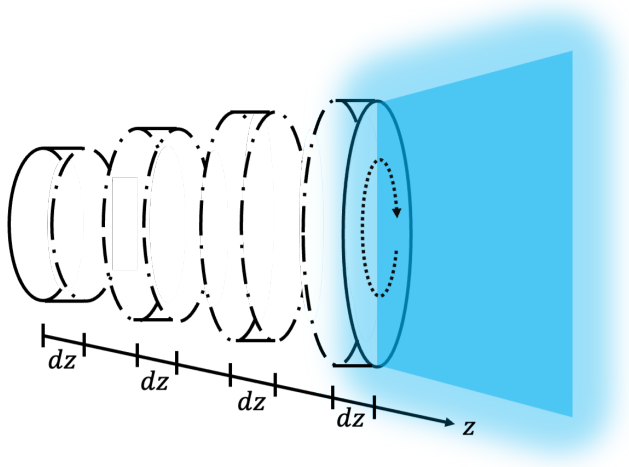

Figure 2: The RMF thruster is modeled to be quasi-1D nozzle with cylindrical cells. Along the central z-axis, each cell has an increasing average radius.

B. Governing Equations

1. Assumptions

We developed a multi-fluid steady state model that includes interactions of the neutrals, electrons, and singly-charged ions. Our approach is based on applying control volume averages over the discretization shown in the previous section to the continuity, momentum, and energy equations. To facilitate this approach, key simplifications we include are:

- Neutral particles experience a constant velocity in the axial direction, $v_{n,z}$, while the velocity contributions in the other directions are neglected,

  $$v_{n,r} = v_{n,\theta} = 0.$$

  Here the radial and azimuthal neutral velocities are $v_{n,r}$ and $v_{n,\theta}$ respectively. We only resolve neutral velocity in the axial direction as their inertia does not allow them to contribute to the azimuthal current on the high frequency time scales associated with the RMF. The neutral radial velocity is also neglected as neutral flux to the walls is reflected back into the geometry. Since the neutral thermal speed is lower than the charged particles bulk speeds, the neutral change in momentum is a negligible effect and the neutral axial velocity is held as constant.

- Ions experience no azimuthal motion as their inertia does not allow them to contribute to the azimuthal current on the high frequency time scales associated with the RMF,

  $$v_{i,\theta} = 0,$$

  where $v_{i,\theta}$ is the ion azimuthal velocity.

- Electrons and ions have the same axial velocity, as we assume local axial ambipolarity. This assumption is justified based on the fact that in a quasi-1D geometry, the total current through a given cross-section

is conserved. As the thruster is self-neutralizing (the cathode only provides seed electrons for igniting the discharge), the total current in the system must be zero:

$$v_{i,z} = v_{e,z} = v_p.$$

Here the axial ion, electron, and plasma velocities are denoted by $v_{i,z}$, $v_{e,z}$, and v_p respectively.

- Ions are cold compared to the electrons such that they experience negligible pressure gradients,

$$\frac{\partial p_i}{\partial r} = \frac{\partial p_i}{\partial \theta} = \frac{\partial p_i}{\partial z} = 0,$$

where p_i is the ion pressure.

- There is a negligible contribution from anistropic electron pressure ($\overleftrightarrow{\Pi}_e$),

$$\vec{\nabla} \cdot \overleftrightarrow{\Pi}_e = 0.$$

- There is no contribution from azimuthal electron pressure gradient to the steady-state solution,

$$\frac{\partial p_e}{\partial \theta} = 0,$$

where p_e denotes the electron pressure. An azimuthal pressure gradient, in the RMF thruster, is a purely high-frequency effect.

- The electron mass is negligible compared to ions and neutrals,

$$\frac{m_e}{m_i} \approx \frac{m_e}{m_n} \ll 1,$$

where m_e, m_i, and m_n are the electron, ion, and neutral xenon particle mass respectively.

- Quasineutrality is conserved,

$$n_e = n_i = n_p,$$

where n_e, n_i, and n_p represent the electron, ion, and plasma number densities respectively.

- Heat flux (θ_e) of the electrons is negligible, as similar to a magnetic nozzle, the plasma is adiabatic-like,[18]

$$\theta_e = 0.$$

We recognize that this assumption is an expedient closure for the electron energy equation.

- The walls of the thruster are electrically isolated, permitting them to float. Consequently, factors associated with wall recombination events are influenced by the dynamics of the plasma sheath.

- Since the high frequency dynamics of the electrons in relation to the RMF occur on a different time scale compared to the steady state fluid model, modifications to the simplifying assumptions are necessary when describing these dynamics in the governing equations.

  - The steady pressure forces, as predicted by the model, are neglected as they are $\sim 40\times$ less than the associated high frequency electric fields. The pressure forces serve to capture the steady state axial ion acceleration dynamics but are not relevant for expressing the azimuthal velocity of the electrons.[17]
  - Electric field axial gradients are much smaller than radial or azimuthal gradients.[17]

2. Continuity Equations

Subject to the preceding assumptions, the control volume analysis over the 1D slices for the conical domain yields for ion and neutral continuity:

$$\frac{\partial}{\partial t}\left[\langle n_p\rangle\langle A\rangle\right]+\frac{\partial}{\partial z}\left[\langle n_p\rangle\langle v_p\rangle\langle A\rangle\right]=\langle A\rangle\left\langle\Gamma^{ion}\right\rangle-\langle A\rangle\left\langle\Gamma^{wall}\right\rangle \tag{1}$$

$$\frac{\partial}{\partial t}\left[\langle n_n\rangle\langle A\rangle\right]+\frac{\partial}{\partial z}\left[\langle n_n\rangle v_n\langle A\rangle\right]=-\langle A\rangle\left\langle\Gamma^{ion}\right\rangle+\langle A\rangle\left\langle\Gamma^{wall}\right\rangle, \tag{2}$$

where A is the cross-sectional area and n_n is the neutral number density. Any term in angled brackets is defined as a cell averaged quantity. We also have defined terms associated with ionization and wall losses:

$$\Gamma^{ion}=\langle n_n\rangle\langle n_i\rangle\langle\sigma_i v_e\rangle \tag{3}$$

$$\Gamma^{wall}=\frac{SA}{V}\langle 0.6n_i\rangle\sqrt{\frac{k_b\langle T_e\rangle}{m_i}}D_B, \tag{4}$$

where $\langle\sigma_i v_e\rangle$ is the ionization reaction rate coefficient for a Maxwellian plasma,[19] SA is the surface area of the cell excluding the end caps, V is the volume of the cell, k_b is the Boltzmann constant, T_e (K) is the electron temperature, and D_B is a magnetic diffusion coefficient:

$$D_B=\frac{\beta_m}{B_{0,\|}^2}. \tag{5}$$

Here β_m is an effective magnetic "confinement" term and $B_{0,\|}$ is the tangential component of the applied magnetic field to the walls. We have in this case, for simplicity, assumed that cross-field transport follows classical diffusion, which dictates that the plasma decay in the presence of a magnetic field exhibits a B^{-2} dependence.[20] In brief, an increasing wall-tangential magnetic field will act to reduce the electron mobility to the walls such that the flux of electrons leaving the system is lower than in an unmagnetized system. Since sheath dynamics enforces that the flux of ions and electrons must be equal, the density of ions reaching the walls is reduced proportionally. Thus, higher magnetic confinement of electrons corresponds to a lower β_m value and thus a lowered density of ions at the wall boundary than that in an unmagnetized system.

3. Momentum Equation

We formulate a momentum equation from the summation of the ion and electron equations:

$$\begin{aligned}\frac{\partial}{\partial t}\left[\langle n_p\rangle\langle v_p\rangle\langle A\rangle\right]+\frac{\partial}{\partial z}\left[\langle n_p\rangle\langle v_p\rangle^2\langle A\rangle\right]&\\ =\left(\frac{e\langle n_p\rangle}{m_i}\langle v_{e,\theta}\rangle B_{r,0}\langle A\rangle\right)+\left(\langle n_p\rangle\langle\nu_{in}\rangle\left(\langle v_p\rangle-\langle v_{n,z}\rangle\right)\langle A\rangle\right)&\\ +\left(\left\langle\Gamma^{ion}\right\rangle\langle v_{n,z}\rangle\langle A\rangle\right)-\left(\left\langle\Gamma^{wall}\right\rangle\langle v_p\rangle\langle A\rangle\right)-\left(\frac{\langle A\rangle}{m_i}\left\langle\frac{\partial p_e}{\partial z}\right\rangle\right),&\end{aligned} \tag{6}$$

where e is the fundamental charge constant and ν_{in} is the collisional frequency between ions and neutrals. The left hand side of Eqn. 6 represents the time rate of change of the momentum, dependent on the source terms on the right hand side of Eqn. 6. Respectively the ion momentum source terms account for axial Lorentz force interaction, the collisional transfer of momentum between ions and neutrals, the momentum transfer from ionization and wall recombination events, and the pressure gradient force.

In order to create a formulation for the azimuthal velocity of the electrons, we look to the high frequency dynamics of the electrons relative to the RMF. Relaying on the high frequency set of simplifying assumptions, we can use Faraday's law of induction to express the time derivative of the magnetic field. Thus, we are able to solve for the high frequency axial electric field,

$$E_{z,1}=\omega r B_\omega\cos(\omega t-\theta), \tag{7}$$

where $E_{z,1}$ is the high-frequency axial electric field, and B_ω is the magnitude of the RMF which oscillates at an angular frequency of ω. Employing a generalized Ohm's law for electrons results in the time-averaged azimuthal electron velocity as

$$\langle v_{e,\theta} \rangle = \frac{2/3\omega R}{1 + 2(B_0^2 + \zeta^2)/B_\omega^2}, \tag{8}$$

where B_0 is the magnitude of the applied magnetic field, and $\zeta = m_e(\nu_{ei} + \nu_{en})/e$ is a collisional drag term. This formulation for the azimuthal electron velocity does not account for the effect of self-induced magnetic fields which serve to cancel out contributions from the applied field. [21] Capturing a closed expression for the contributions of the self-induced magnetic field is not numerically tractable in this simplified model. [22] Thus, we include the addition of the coefficient, σ, which acts to encapsulate this phenomenon. Eqn. 8 is now re-written as

$$\langle v_{e,\theta} \rangle = \frac{2/3\omega R}{1 + 2(B_0^2 + \zeta^2)/(\sigma B_\omega)^2}. \tag{9}$$

This expression shows that as the strength of applied field is increased, the electrons become more strongly tied to the applied field and thus experience less entertainment to RMF, lowering the drift velocity. In essence, the applied field and heavy particle collisions apply a drag force to the azimuthal electron motion. Additionally, at an increasing thruster radius, the drift velocity increases as the electrons must move faster to sustain the same angular frequency.

4. Electron Energy Equation

The electron pressure is updated via the electron internal energy equation,

$$\begin{aligned}\frac{\partial}{\partial t}\left[\left\langle \frac{3}{2}p_e \right\rangle \langle A \rangle\right] + \frac{\partial}{\partial z}\left[\left\langle \frac{5}{2}p_e \right\rangle \langle v_p \rangle \langle A \rangle\right] \\ = -\langle en_p \rangle \langle v_p \rangle \langle E_{z,0} \rangle \langle A \rangle - \langle en_p \rangle \langle v_{e,\theta} \rangle \langle E_{\theta,0} \rangle \langle A \rangle + \langle P_{heat} \rangle \langle A \rangle - \left\langle \Gamma^{ion} \phi_{ion} \right\rangle \langle A \rangle \\ - \langle \Gamma_{en}^{exc} \rangle \langle \phi_{exc,en} \rangle \langle A \rangle - \langle \Gamma_{ei}^{exc} \rangle \langle \phi_{exc,ei} \rangle \langle A \rangle - \left\langle \Gamma^{wall} \right\rangle \langle \phi_{wall} \rangle \langle A \rangle,\end{aligned} \tag{10}$$

where ϕ_{ion} is the energy loss associated with a single ionization event, Γ_{en}^{exc} is the excitation reaction rate between electrons and neutrals, $\phi_{exc,en}$ is the energy loss associated with a single electron/neutral excitation event, Γ_{ei}^{exc} is the excitation reaction rate between electrons and ions, and $\phi_{exc,ei}$ is the energy loss associated with a single electron/ion excitation event. The steady axial electric field ($E_{z,0}$), derived from a time-averaged Ohm's Law, is expressed as

$$E_{z,0} = v_{e,\theta} B_r - \frac{1}{en_e}\frac{\partial p_e}{\partial z} - \frac{m_e}{e}\nu_{en}(v_{e,z} - v_{n,z}). \tag{11}$$

Similarly, the steady azimuthal electric field ($E_{\theta,0}$) is

$$E_{\theta,0} = -v_{e,z} B_r - \frac{m_e}{e} v_{e,\theta}(\nu_{ei} + \nu_{en}). \tag{12}$$

The energy loss to the wall is dependent on sheath dynamics such that the internal energy loss as the electrons leave the domain across the sheath edge is given by [19]

$$\phi_{wall} = \frac{k_b T_e}{e}(2 + \ln\left[\sqrt{\frac{2m_i}{\pi m_e}}\right]). \tag{13}$$

The excitation energy loss rate term is

$$\Gamma_{ss'}^{exc} = \langle n_s \rangle \langle n_s' \rangle \langle \sigma_{exc} v_s \rangle, \tag{14}$$

where $\langle \sigma_{exc} v_s \rangle$ is the excitation reaction rate coefficient for a Maxwellian plasma. [19] The Ohmic heating term (P_{heat}) resulting from the high frequency time varying electric field is, [17]

$$\langle P_{heat} \rangle = \frac{\pi \left(e\omega B_\omega\right)^2 \langle R \rangle^4 n_p}{4 m_e \nu_a \langle A \rangle}\left(1 - \frac{1}{1 + 2(B_0^2 + \zeta^2)/(\sigma B_\omega)^2}\right), \tag{15}$$

where ν_a is a coefficient representing the anomalous collision frequency of the electron motion azimuthally.

When substituted into Eqn. 10, the first term of Eqn. 11 represents cooling as the plasma is accelerated out of the domain. The second term also represents cooling through the expansion of the plasma through the expanding conical geometry, and the third term represents heating through collisional drag. Similarly, when Eqn. 12 is substituted into Eqn. 10, the first term represents an RMF heating mechanism, and the second term represents Ohmic heating from elastic collisions. Due to the high frequency of the RMF, classical values of the collision frequencies are orders of magnitude too low to capture the correct effect of the high frequency Ohmic heating, P_{heat}. One possible explanation is wave-particle interactions resulting in a substantial contribution to an increased collision frequency.[23,24] However, as this underlying physical phenomenon is still an open question, we include the constant anomalous collision frequency in Eqn. 15 to encapsulate this phenomenon. Additionally, of particular note, is the interplay between the P_{heat} (Eqn. 15) and $v_{e,\theta}$ (Eqn. 9) formulations relative to the Hall parameter term in parenthesis. Increasing this parenthetical term provides an increase in Lorentz force and reduces Ohmic heating.

C. Numerical Techniques

In order for the successful operation of this finite volume method simulation, there are are number of numerical techniques that needed to be considered including domain initialization, the flux residual calculation, and the cell update process.

1. Domain Initialization

While the governing equations ultimately dictate the steady state solution, we must initialize the model domain to a prescribed starting point to ensure numerical stability. This is achieved through the use of restart files from previously converged solutions.

2. Flux Residual Calculation

The state in each cell, stored at cell center, for the neutral continuity, plasma continuity, plasma momentum, and plasma energy equations are respectively

$$U = \left[\; n_n A \;\middle|\; n_p A \;\middle|\; n_p v_p A \;\middle|\; \tfrac{3}{2} p_e A \; \right]. \tag{16}$$

The flux in each cell for the neutral continuity, plasma continuity, plasma momentum, and plasma energy equations are respectively

$$F = \left[\; n_n v_n A \;\middle|\; n_p v_p A \;\middle|\; n_p v_p^2 A + p_e A \;\middle|\; \tfrac{5}{2} p_e v_p A \; \right]. \tag{17}$$

We utilized a Russonov flux formulation to calculate the flux across cell boundaries, owing to the numerical simplicity of the flux. The form of this flux is,

$$\hat{\mathbf{F}} = \frac{1}{2}\Big(\mathbf{F}_L + \mathbf{F}_R\Big) - \frac{1}{2} s_{max}\Big(\mathbf{U}_R - \mathbf{U}_L\Big), \tag{18}$$

where U_L is the left-hand cell state, U_R is the right-hand cell state, $F_L = F(u_L)$ is the cell centered flux of the left-hand cell, $F_R = F(u_R)$ is the cell centered flux of the right-hand cell, and s_{max} is the maximum propagation speed of the ion acoustic waves within the system considering both u_L and u_R. This maximum propagation speed is calculated as

$$s_{max} = max\left\{s_{max,L}, s_{max_R}\right\} = max\left\{\left|v_{p,L} \pm c_L\right|, \left|v_{p,R} \pm c_R\right|\right\} \tag{19}$$

where the ion sound speed (c) is defined as $c = \sqrt{\gamma p_e / n_p m_i}$, and $\gamma = 5/3$ is the specific heat capacity ratio. Interior to the domain, the calculations for the relevant flux use the cells left and right of the cell boundary. However, at the inflow and outflow boundaries, the left-most and right-most cell are ghost cells. The ghost cells are additional numerical cells that extend beyond the physical domain such that the required boundary conditions are satisfied. At the upstream boundary, we implement the introduction of neutral gas flow through a Dirichlet ghost cell, where we set the gas inflow equal to an experimentally measured mass flow rate. For all data points we considered during model calibration, we held the gas injected into the device at a constant flow rate. The ghost-cell states associated with plasma species are calculated

from a linear extrapolation of the last two cells interior to the domain. Subsequently, we added back into the neutral density population, at the neutral thermal speed, the ion mass flow exiting at the upstream boundary. This serves to represent the recombination of the plasma species into neutral particles at the backwall. At the outflow boundary, we treat all the ghost cell states through a linear extrapolation of the last two cells interior to the domain. This specific linear extrapolation implementation of the ghost cells represents supersonic inflow and outflow conditions.[25]

3. Cell Update

The residual of each cell (R) is calculated as

$$R = -dt\left(\frac{\hat{F}_R - \hat{F}_L}{dz} + S_{plasma} + S_{area}\right), \tag{20}$$

where $\hat{F}_R$ is the nominal Rusonov flux at the right-hand boundary, $\hat{F}_L$ is the nominal Rusonov flux at the left-hand boundary, S_{plasma} is the source terms due to RMF axial and azimuthal electric fields and inelastic collision processes, and S_{area} are the source terms associated with the area expansion of the thruster geometry. S_{plasma} and S_{area} are all terms on the right-hand side of the governing equations. A local timestep,

$$dt = 0.45\frac{dz}{s_{max}}, \tag{21}$$

calculated for each cell, dynamically adapts. The leading constant is necessary for numerical stability of the system. The model then updates the states by summing the current state value and the residual value in each cell,

$$U_{new} = U_{current} + R, \tag{22}$$

where $U_{current}$ is the current state, and U_{new} is the updated state, both defined at the cell center. This update step incrementally moves the solution towards convergence. To determine when a steady state solution is reached, we scale the cell's residual by the updated state. If this scaled residual falls within the user-defined convergence criteria, we consider the model to be converged to its steady state value. The model then uses this converged state to calculate performance metrics. We consider the solution converged when the L2 residual norm, which measures an average error across all cells, falls below the threshold of 1×10^{-4}.

IV. Relating Model Outputs to Thruster Performance Metrics

In this section, we introduce how the model outputs predictive thrust and plasma coupled power measurements. We also introduce an efficiency model to capture the contribution of the power loss mechanisms in the thruster and their relative impact on overall thruster performance.

A. Thrust Prediction

Upon convergence, the model uses the steady-state flow field to compute the thrust produced. This value predicted by the model is formulated as

$$F_T = \cos(\theta_d)(\rho_p u_p^2 A)_{exit}, \tag{23}$$

where F_T is the model predicted thrust and θ_d is the divergence angle of the plume.

B. Efficiency Model

We established an overall efficiency model to better understand the individual loss processes internal to the RMF thruster. The total efficiency is determined by multiplying its constituent components,

$$\eta = \eta_p \eta_m \eta_d \eta_c = \eta_c \eta_{post}, \tag{24}$$

where η denotes the overall thruster efficiency, η_p is the plasma efficiency, η_m is the mass utilization efficiency, η_d is the divergence efficiency, η_c is the coupling efficiency, and η_{post} is the post coupling thruster efficiency. We provide more detail on each of these modes in the following subsections.

1. Plasma Efficiency

The plasma efficiency (η_p) indicates the fraction of coupled power that is converted into thrust in comparison to the total power coupled into the plasma. This efficiency is defined mathematically as

$$\eta_p = \frac{P_{mom}}{P_p}. \tag{25}$$

The power absorbed by the plasma ("plasma power" or "plasma coupled power") in the domain is

$$P_p = P_{mom} + \sum_{dz}^{L} \left[v_p \frac{\partial p_e}{\partial z} A dz + m_e n_p \left[(v_p^2 - v_p v_n + v_{e,\theta}^2)\nu_{en} + v_{e,\theta}^2 \nu_{ei} \right] A dz + P_{heat} A dz \right]. \tag{26}$$

where the terms in the brackets result from the steady axial and azimuthal electric field contributions to the electron energy equation. The second term in Eqn. 26 represents the power associated with pressure gradient of the plasma. The third term and fourth terms represent the heating due to particle collisions. The total power absorbed by the plasma is therefore the sum of the power absorbed in each cell throughout the entire thruster domain in addition to the momentum power, P_{mom}, at the exit plane. P_{mom} also defined as the power associated with the thrust, is calculated using the expression,

$$P_{mom} = \frac{1}{2}(\dot{m}_p v_p^2)_{exit}, \tag{27}$$

where $\dot{m}_{p,exit}$ denotes the mass flow rate of the plasma species at the thruster exit plane.

2. Mass Utilization Efficiency

The mass utilization efficiency (η_m) quantifies the efficiency with which the neutral particles are ionized within the thruster. It is mathematically expressed as

$$\eta_m = \frac{\dot{m}_{p,exit}}{\dot{m}_{in}}, \tag{28}$$

where $\dot{m}_{in}$ is the total inflow mass flow rate.

3. Divergence Efficiency

The divergence efficiency (η_d) reflects the degree with which the plasma plume is collimated as it exits the thruster. It is quantitatively defined as

$$\eta_d = \cos^2(\theta_d). \tag{29}$$

Since the model does not self-consistently predict the divergence angle of the plume, it is thus treated as a free parameter within the model.

4. Coupling Efficiency

The coupling efficiency (η_c) quantifies the effectiveness of the power processing unit (PPU) to deliver power to the plasma via the antennas. As the model is independent of the power process unit (PPU), the coupling efficiency is not estimated by the model. Regardless, this efficiency is mathematically expressed as

$$\eta_c = \frac{P_p}{P_{PPU}}, \tag{30}$$

where P_{PPU} is the power supplied into the power processing unit.

5. Post Coupling Efficiency

The post coupling efficiency (η_{post}) indicates the overall thruster efficiency disregarding the power losses associated with coupling power between the PPU and plasma, via the antennas. This efficiency is

$$\eta_{post} = \eta_p \eta_m \eta_d = \frac{F_T^2}{2\dot{m}_{in} P_p}. \tag{31}$$

6. Inelastic Processes Power Fractions

We performed a detailed analysis of the power loss components, in order to determine the dominant inelastic loss process,

$$P_{process} = P_{mom} + P_{exc} + P_{wall} + P_{ion} + P_{th,inlet} + P_{th,exit}, \tag{32}$$

where P_{exc}, P_{wall}, P_{ion}, $P_{th,inlet}$, and $P_{th,exit}$ symbolize the power loss due to excitation, wall recombination, ionization, residual thermal energy at the backwall, and the residual thermal energy at the thruster exit respectively. The power losses associated within the internal domain (excitation, wall, and ionization losses) are calculated by taking the summation of the power loss in each cell over the entire length of the thruster:

$$P_{exc} = \sum_{dz}^{L} \Gamma_{rad}\phi_{rad}Adz \tag{33}$$

$$P_{wall} = \sum_{dz}^{L} \Gamma_{wall}\phi_{wall}Adz \tag{34}$$

$$P_{ion} = \sum_{dz}^{L} \Gamma_{ion}\phi_{ion}Adz \tag{35}$$

The residual thermal energy power loss associated with the domain boundaries are taken to be the Rusanov flux of the internal energy between the interior domain and the ghost cells at the respective locations. The relative contribution of each power loss process, $P_{process}$, to the total plasma power is characterized by

$$\alpha_{process} = \frac{P_{process}}{P_p}. \tag{36}$$

By evaluating the power loss fraction, α, for each inelastic collision process, we formulate a deeper understanding into the distribution and utilization of the plasma coupled power.

V. Model Calibration

In this section, we introduce the experimental setup and the conditions relevant to the collected experimental data used to calibrate the model free parameters. We will also explicitly define the model free parameters and outline the Bayesian inference approach that was used to calibrate them.

A. Test Article

This experiment was conducted in the Alec D. Gallimore Large Vacuum Test Facility (LVTF) at the University of Michigan's Plasmadynamics and Electric Propulsion Laboratory. Fig 3 shows the RMF v3 test article which obtains its conical geometry from a Pyrex glass plasma-bounding cone. We note here that while the plasma-bounding cone is curved for the actual device, for simplicity in the quasi-1D modeling implementation, we calculated a cone half-angle via measuring the initial and final thruster radius. Tuning capacitors mounted behind the backplate of the thruster ensure that the antennas fire at the correct frequency, and three sets of two-phase antennas are wound in a saddle-like loop pattern along the body of the plasma-bounding cone which generate the RMF within the device. An applied-magnetic field is created by a pair of solenoids (or bias magnets). These solenoids are comprised of magnet wire wound on a circular aluminum structure and connected via rods to an aluminum backplate. Seed plasma is provided by an externally mounted LaB_6 cathode such that cathode inlet flow is injected back into the thruster body. Neutral gas is also separately introduced at the backwall, within the plasma bounding cone, via a circular injector.

B. Operating Conditions and Experimentally-Generated Data

Table 1 lists the geometry of the RMF v3 thruster, the neutral injected flow rate, and the applied and RMF field strengths associated with the experimental thrust and plasma-coupled power measurements gathered. The RMF v3 thruster was operated in a continuous wave mode to obtain thrust measurements using an inverted pendulum thrust stand. Plasma coupled power is calculated by comparing antenna waveform traces

between vacuum shots and plasma-loaded shots in order to determine the amount of power coupled into the plasma. More details in regards to the experimental test campaign and the associated data can be found in Ref [17].

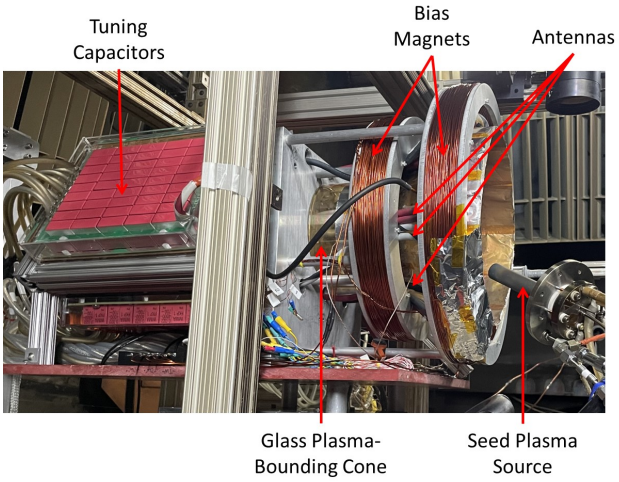

Figure 3: The RMF v3 test article in the Large Vacuum Test Facility at the University of Michigan.

C. Model Parameters

In order to leverage this computational framework for thruster performance insights and design trade studies, there are a number of unknown coefficients that must be tuned to calibrate the accurateness of the model to experimental data. The free parameters are the magnetic confinement factor dictating ion flux to the walls (β_m), the induced magnetic field factor (σ), the high frequency anomalous collision frequency (ν_a), and the plume divergence angle (θ_d). Table 1 summarizes the model free parameters, their physical bounds, and there associated dependencies within the model.

D. Bayesian Inference to Determine Free Parameters

Due to the low fidelity of the one-dimensional model, there are inherent limitations in regards to its accuracy of performance predictions. Thus, we must tune the free parameters so that the model is able to recreate experimental thrust and plasma power measurements at given applied magnetic field strengths.

In order to gain these calibrated free parameters, we employ Markov Chain Monte Carlo (MCMC), a set of algorithms aimed at sampling from arbitrary distributions to create posterior distributions. The goal of MCMC, when applied to Bayesian inference, is to sample from the posterior distribution of the model. The sampler works by first generating a proposed set of free parameters, running the model, and generating a predicted thrust and plasma power value. The sampler then evaluates the acceptance probability of moving from an accepted set of free parameters to the proposed set based how closely the model performance predictions compare to the experimental data. The sampler will only move to the proposed set if the acceptance probability is above a certain threshold. If a proposed sample has a free parameter outside its given physical bounds, the acceptance probability is set to zero. We are thus able to explore the posterior distribution of the model and generate sets of free parameters that allow the model to accurately predict thruster performance.

The specific MCMC algorithm chosen was Delayed Rejection Adaptive Metropolis (DRAM). If a sample is initially rejected, the delayed rejection portion of the algorithm proposes a secondary sample based on the initially rejected sample location before moving on in the sampling process. The adaptive metropolis portion of the algorithm recursively updates the covariance matrix, used to generate proposed samples, based on the ever-growing set of accepted samples.

E. Summary of Parameters

Table 1 lists all the associated experimental, learned, and output parameters necessary to run the one-dimensional model.

Parameter Type	Parameter Name	Symbol	Numerical Value	Units
Model Input	Thruster Length	L	0.11	m
Model Input	Initial Thruster Radius	r_0	0.07	m
Model Input	Cone Half Angle	θ_{cone}	46.4	deg
Model Input	Injector Mass Flow Rate	$\dot{m}_{inj}$	272	sccm
Model Input	Neutral Thermal Speed	v_n	150	m/s
Model Input	Applied Radial Bias Field Strength	B_{r0}	23.01, 28.78, 34.50, & 40.30	G
Model Input	Applied Axial Bias Field Strength	B_{z0}	73.82, 92.38, 110.77, & 129.24	G
Model Input	Rotating Magnetic Field Strength	B_ω	20.46	G
Model Input	Rotating Magnetic Field Frequency	f_{RMF}	413.2	kHz
Learned	Wall Confinement Coefficient (Dependent Calculation = Γ_{wall})	β_m	$0 \rightarrow \infty$	G^2
Learned	Anomalous Azimuthal Collision Frequency (Dependent Calculation = P_{heat})	ν_a	$0 \rightarrow \infty$	s^{-1}
Learned	Induced Magnetic Field Factor (Dependent Calculation = $v_{e,\theta}$ & P_{heat})	σ	$0 \rightarrow \infty$	–
Learned	Plume Divergence Angle (Dependent Calculation = F_T & η_d)	θ_d	$0 \rightarrow 90$	deg
Model Output	Thrust	F_T	–	mN
Model Output	Plasma Coupled Power	P_p	–	kW

Table 1: A summary of all the experimental, learned model, and output model parameters associated with model calibration process.

VI. Results

In this section, we present an analysis indicating how accurately the calibrated model predicts thrust and plasma coupled power. We then show a comparison between the model predicted and experimentally determined efficiency metrics. The section concludes by exhibiting the model predicted power fractions, Eqn. 36, which give insight into the dominant loss mechanisms of the thruster.

A. Model to Experimental Results Comparison

Figures 4a and 4b show, respectively, a comparison between the experimentally measured and model predicted thrust and plasma coupled power. We can see that the calibrated model is able to recreate the experimental thrust measurements within the uncertainty bounds. The calibrated model similarly matches the increase in plasma coupled power with applied field strength. For both the thrust and power results, we note there are trends in the experimentally-measured median values that are not captured by the model median values. However, the predictions in all cases remain within experimental uncertainty, and thus these deviations may not be statistically significantly. We proceed then in the following under the assumption that the model is sufficiently calibrated to extract insights into the efficiency modes driving the thruster operation.

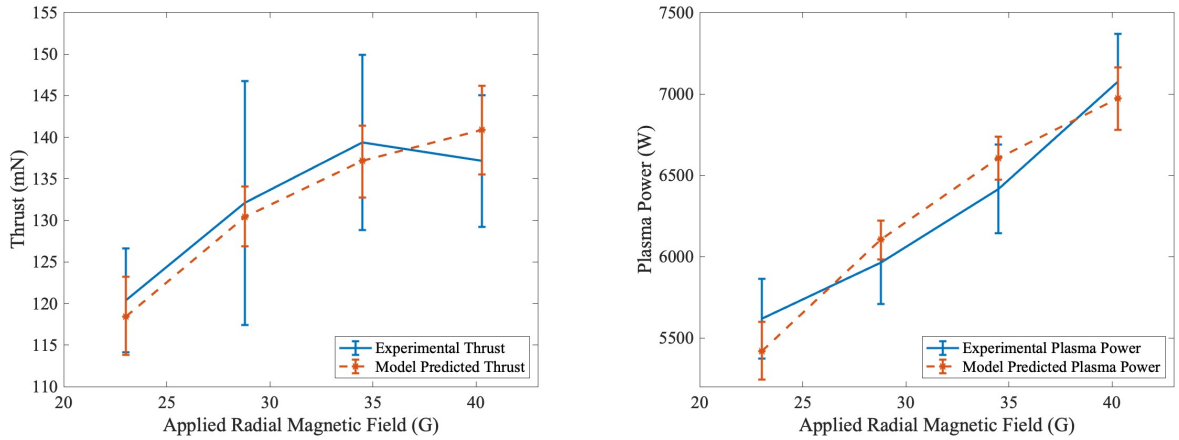

(a) (b)

Figure 4: A comparison of (a) thrust and (b) plasma coupled power values between the experimental data and the calibrated model results over a range of applied magnetic field strengths.

B. Model Validation Through Efficiency Modes Comparison

Fig 5a shows the mass utilization, divergence, and plasma efficiency, while Fig 5b shows post coupling efficiency all plotted against the experimental applied field magnitudes. The coupling efficiency is not calculated as the model simulates thruster dynamics and does not account for PPU losses.

Overall, our results indicate that the predominant loss process is the plasma efficiency, consistent with previous experimental work (See Ref [17]). The model predicts an average plasma efficiency of $16.5 \pm 2.3\%$ comparable to an experimentally measured plasma efficiency, at a lower power condition, of $9.6 \pm 2.3\%$. Plasma efficiency increases with applied field strengths, as the axial Lorentz force driving plasma acceleration strengths. Under the assumption of singly charged ions, the model calculates that mass utilization is on average $88.8 \pm 1.1\%$. This is a slight decrease from $98 \pm 8\%$ measured experimentally, at a lower power condition, but not a major driver to explain poor performance. In terms of the divergence efficiency, the model predicts an average of $40.0 \pm 6.1\%$, corresponding to a divergence angle of $50.8 \pm 3.6°$ consistent with experimental probe measurements conducted at lower powers.[17] Fig 5b corroborates the accuracy of our calibrated model, showing a comparison between experimental measurements of the post coupling efficiency and model predictions, as the model predictions for post coupling efficiencies fall within the experimental uncertainty bounds.

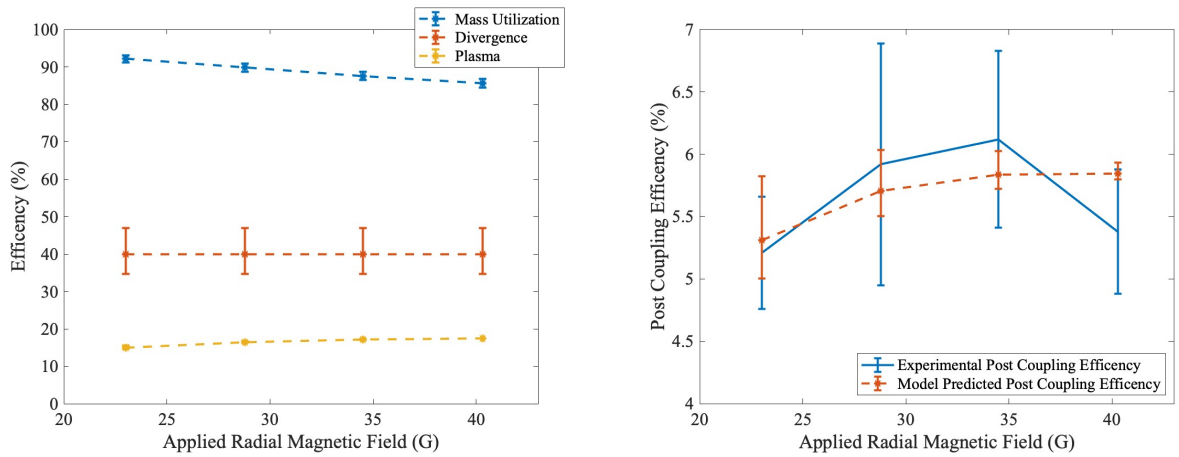

(a) Mass Utilization, Divergence, and Plasma Efficiency

(b) Post Coupling Efficiency

Figure 5: Model predictions of the (a) mass utilization, divergence, and plasma efficiencies for the experimental data set used for model calibration. (b) Model predicted values vs. experimental measurements of the post coupling efficiency.

C. Power Fractions Breakdown

Armed with the insight from the previous section, that the plasma efficiency is the dominant loss mechanism in the system, we turn here to investigating the processes that drive this low efficiency. To this end, we show in Fig 6 for the applied field conditions used to calibrated the model, the breakdown in plasma power as distributed amongst useful power (momentum power) and the power loss processes.

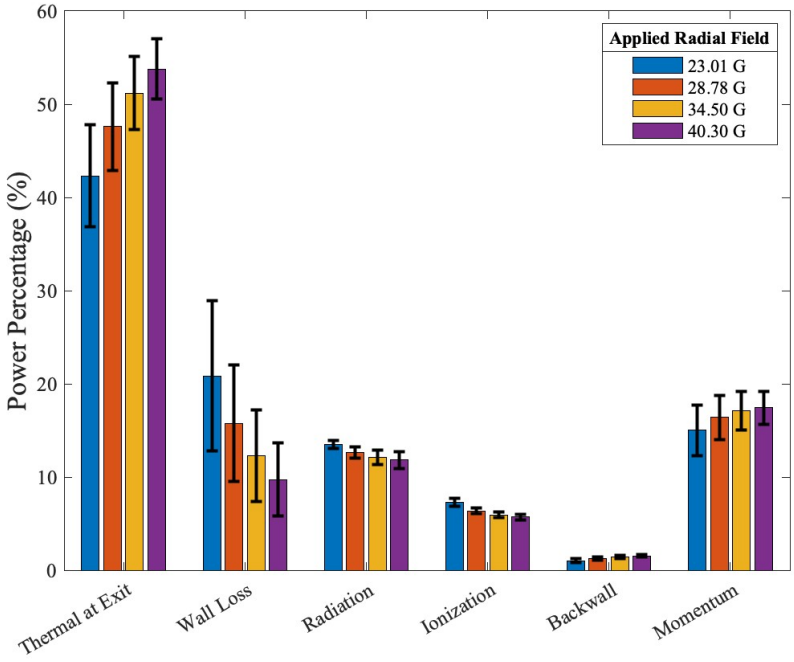

Figure 6: Constituent contributions to the plasma power as inferred from the model for different applied magnetic field strengths.

The first result we note is that the residual thermal energy at the thruster exit. At higher applied field strengths, the residual thermal energy power loss increases. This stems from Eqn. 15, which indicates that at higher applied field strengths electrons experience a larger drag force, become less entrained to the RMF, causing increased heating of the plasma. The residual thermal energy at the thruster exit has the largest contribution to the plasma power, accounting for $42 - 54\%$ over the applied field conditions, due to high predictions for the electron temperatures. Fig 7 shows that the model predicts a sharp increase in electron temperature throughout the domain resulting in $\sim$ 95eV electrons at the exit plane for the strongest applied field case. We believe these high electron temperatures are non-physical as secondary inelastic loss processes such as secondary ionization and the activation of higher excitation states will commence which will constrain the electron temperature. This would serve to increase the constituent contributions of other loss processes to the plasma coupled power but reduce the residual thermal energy lost at the thruster exit. We discuss the reasoning behind the overestimate in predicted electron temperatures in Discussion Section D.

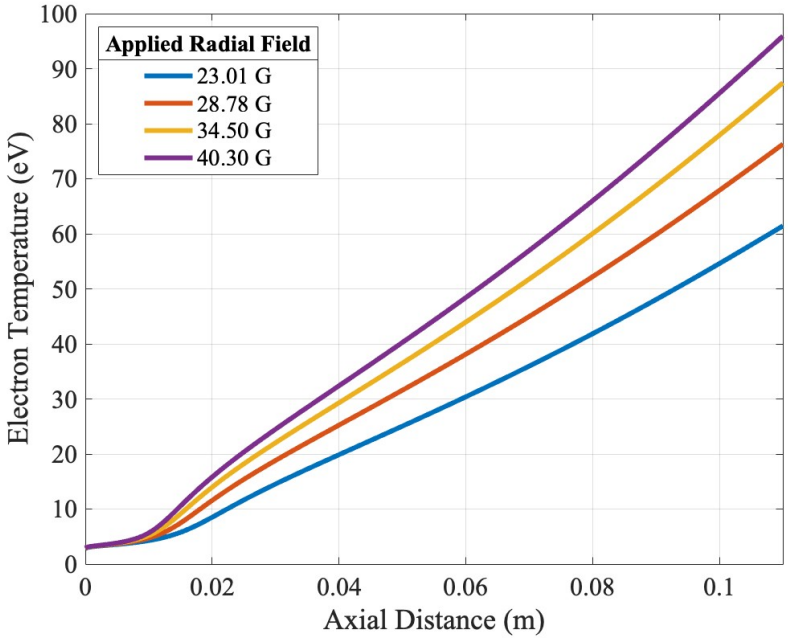

Figure 7: An axial profile of the electron temperatures at increasing applied field strengths.

After the residual thermal losses, the next dominant loss is power to the walls, amounting for at most 20.8% of the plasma power. Physically, this result stems from the fact that as charged particles stream to the walls, through the sheath boundary, they remove energy from the plasma. The power to the walls is reduced with increasing applied magnetic field due to the enhanced effective magnetic confinement of electrons.

The radiation and ionization losses are comparable to the wall losses in the system, though we remark that in a departure from previous pulsed work performed on a similarly configured thruster,[15] these radiative losses are not the dominant mechanism. This is further validation that the CW method serves to mitigate this loss process. With increasing applied field strengths, due to greater Lorentz forces, ions are accelerated to higher speed. This lowers the average plasma density in the system, commensurately lowering radiation and ionization losses but also decreasing mass utilization efficiency.

We also observe that the backwall losses are negligible. This stems from the fact that at the backwall, the electron temperatures and associated Bohm speeds dictating this power loss are low. The primary RMF heating mechanism contributing to this, the high frequency Ohmic heating term (P_{heat}), is relatively small near the backwall since this term is dependent on the thruster radius to the fourth power (Eqn. 15). With increasing applied field strengths we also notice that backwall losses increase slightly as higher average electron temperatures are associated with higher applied field cases.

As a final note, we show here that the useful momentum power increases with increasing applied field. This likely can be explained by the fact that the axial Lorentz force driving plasma acceleration is enhanced with increased applied field.

In summary, from the above analysis, we find that the residual thermal energy at thruster exit is the primary contribution to power loss. However, overestimates in electron temperatures would cause the proportional contributions of the lesser power loss processes to grow. Overall, the momentum power remained at less than 20% across all applied field conditions, which correlates to the low plasma efficiencies predicted by the model.

VII. Discussion

In this section we start by analyzing a posterior free parameter sample to gain insights into the RMF operation. We then use the calibrated model to perform three design studies and model-driven global design optimization that all serve to inform the design of a future RMF test article. We conclude this section by mentioning the known model limitations and their effect on performance predictions.

A. Physical Interpretation of the Maximum Likelihood Estimation Free Parameter Set

We take one sample from the posterior distribution, listed in Table 2, in order to illustrate the effects of the model free parameters values on the RMF thruster operation. We will refer to this posterior sample as the maximum likelihood estimation (MLE) point, as it represents the set of free parameters with which the model most accurately recreates the experimental data. The full plots of the 1-D and 2-D marginals of the free parameters are presented in Appendix A.

As the magnetic field wall confinement factor (β_m) is dependent on the tangential component of the applied field at the wall, the flux of ions to the walls is also dependent on the total applied field strength. Between the experimental cases where $B_{r,0}$ was 23.01 G, 28.78 G, 34.50 G, and 40.30 G, the posterior sample represents an ion flux reduction to the walls of 67%, 79%, 85%, and 89% respectively. These relatively high reductions in the ion fluxes help to minimize the power lost to the wall.

The posterior sample of the self-induced field coefficient (σ) indicates that the magnitude of applied field is decreased by 2.67× due to the imposing contributions of the self-induced magnetic field. This effective decrease in the applied magnetic field strength increases the azimuthal electron velocity as electrons experience less drag forces and instead rotate more synchronously with the the applied RMF frequency. This also serves to decrease the high frequency Ohmic heating term.

The high frequency anomalous collision frequency (ν_a) sample suggests a frequency equal to 1.40×10^{10} s^{-1}. This is $\sim 10,000\times$ larger than classical collision frequencies accounting for heavy particle interactions within the thruster. Anomalous frequencies in Hall thruster models, however, are typically only $10 - 100\times$ larger.[24] One explanation is the effect of wave-particle interactions which would decrease the electron resistivity within the device and effectively serve to increase the anomalous collision frequency term.[23,24] In terms of this free parameter effecting the model predictions, Fig 4b demonstrated that the calibrated model does not correctly capture the inflection of the plasma power curve seen experimentally. This is likely due to the assumption of a constant high frequency anomalous collision frequency across all the experimental data points. Adding fidelity to the formulation of this parameter, for example a dependence on electron temperature, could better allow the model to capture the correct slope of the plasma power trends.

The posterior sample for the divergence angle (θ_d) is nearly identical to probe measurements, conducted at a lower power condition, which specified a divergence angle of 45°.[17] The assumption of a constant plume divergence angle coefficient, could explain why the calibrated model is unable to capture the experimental optimum thrust value seen in Fig 4a. Increases in applied field strengths, could serve to enhance beam collimation. This added level of model fidelity could help match experimental data further by allowing for more fine tuning of the self-field coefficient which, we conjecture, dictates the location of the optimum thrust value seen experimentally.

Free Parameter	Symbol	Posterior Sample
Wall Confinement Factor	β_m	20.04 G^2
Induced Magnetic Field Factor	σ	2.67
Anomalous Azimuthal Collision Frequency	ν_a	1.37×10^{10} s^{-1}
Plume Divergence Angle	θ_d	48.79 deg

Table 2: A free parameter posterior sample of the calibrated one-dimensional RMF thruster model.

B. RMF Thruster Design Trade Study

Now with the calibrated model in hand, we are able to leverage this tool in order to perform trade studies to motivate the next design iteration of the RMF thruster. To this end, three trade studies were performed in which the injector mass flow rate was held constant at its experimental value and the MLE-values were used as the model free parameter set.

1. Angular Geometry Trade Study

As our results from the preceding analysis have shown, in order to overcome the low plasma efficiency for this system, the primary mode we need to target is plasma efficiency. To address this, we start by identify designs that either reduce wall losses or facilitate higher Lorentz driven acceleration in the device. This motivates our first parametric study in which we vary the half cone angle and the relative angle of the magnetic field. The former will serve to reduce wall losses by allowing for a larger aperture of the system. As we assume that the initial radius of the device is constant, increasing the half angle also has the effect of leading to a larger average radius of the device. This in principle can enhance the Lorentz force as the electron current (Eqn. 9) scales with the device size. Increasing the relative contribution of the radial component of the magnetic field in principle also has the effect of enhancing the Lorentz acceleration (Eqn. 6).

To highlight these trades quantitatively, we show in Figures 8a, 8b, and 8c parametric plots for the plasma, mass utilization, and post coupling efficiency of the system. To generate these results, we have assumed the a constant total applied field strength of 135 G. The trends in the plasma efficiency largely support the preceding interpretation for how plasma efficiency will improve with both radial component and half angle of the thruster. The results suggest that both should be approximately maximized, enabling plasma efficiencies as high as 30%. Physically, the thruster geometry that would emerged from this type of variation would start to appear planar with a predominately radial magnetic field tangent to the surface. This is a notable result as it broadly mirrors the configuration of planar inductive thrusters that have been explored in previous work.[26] We note here that these improvements in plasma efficiency generally translate to increases in the overall efficiency of the system. This is captured in Fig 8c.

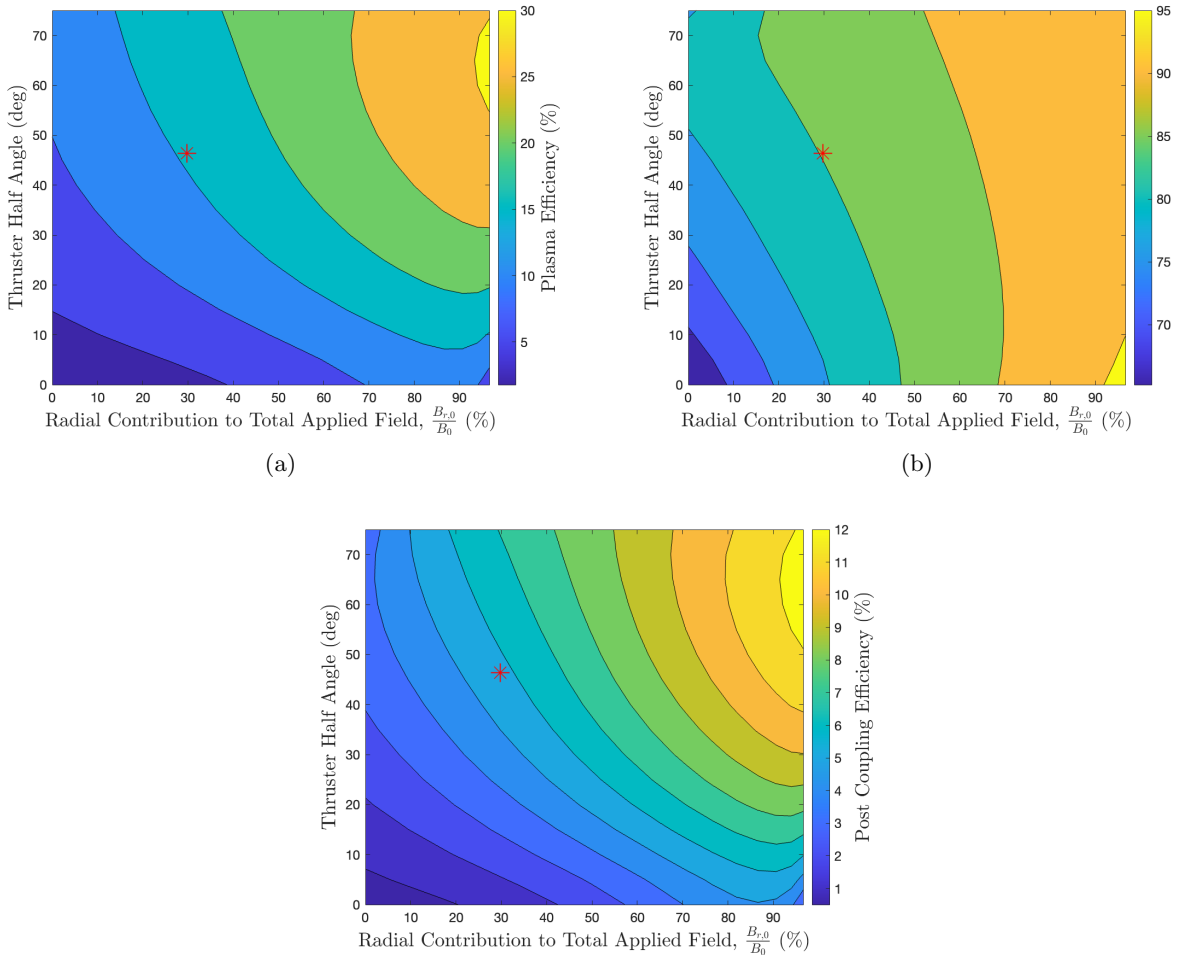

Figure 8: (a) Plasma, (b) mass utilization, and (c) post-coupling efficiency results of a trade study comparing the contributions of the bias field components to the thruster half angle. The location of the experimental calibration data is indicated by the red asterisk marker.

2. Length Scale Trade Study

Another potential method for improving thruster performance is to increase the length scale and radius. Given that the Lorentz force is a volumetrically acting force, increasing the dimensions of the thruster, in principle, will allow for an enhanced contribution of this effect. To evaluate this parametrically, Fig 9a and 9c show the plasma and post coupling efficiencies as we vary the length and radius of the thruster. In this case, we have fixed the cone angle of the thruster to 46.4°.

As in the preceding section, we find that both of these factors improve plasma efficiency of the system, though with not the same combined effect as adjusting cone angle and radial component of the magnetic field. Although the plasma efficiency increases for this result, in a departure from the previous section, the overall thruster efficiency does not exactly mirror the plasma efficiency. This suggests other efficiency modes suffer. To this point, we show in Fig 9b the variation in mass utilization. This result can be explained intuitively by the fact that as the thruster radius and length increase, the effective plasma density and neutral density in the system decrease, resulting in lower ionization rates in the acceleration region. As a result of this trade, we anticipate that simply scaling the current device to larger size is not a viable design improvement without also altering mass flow rates.

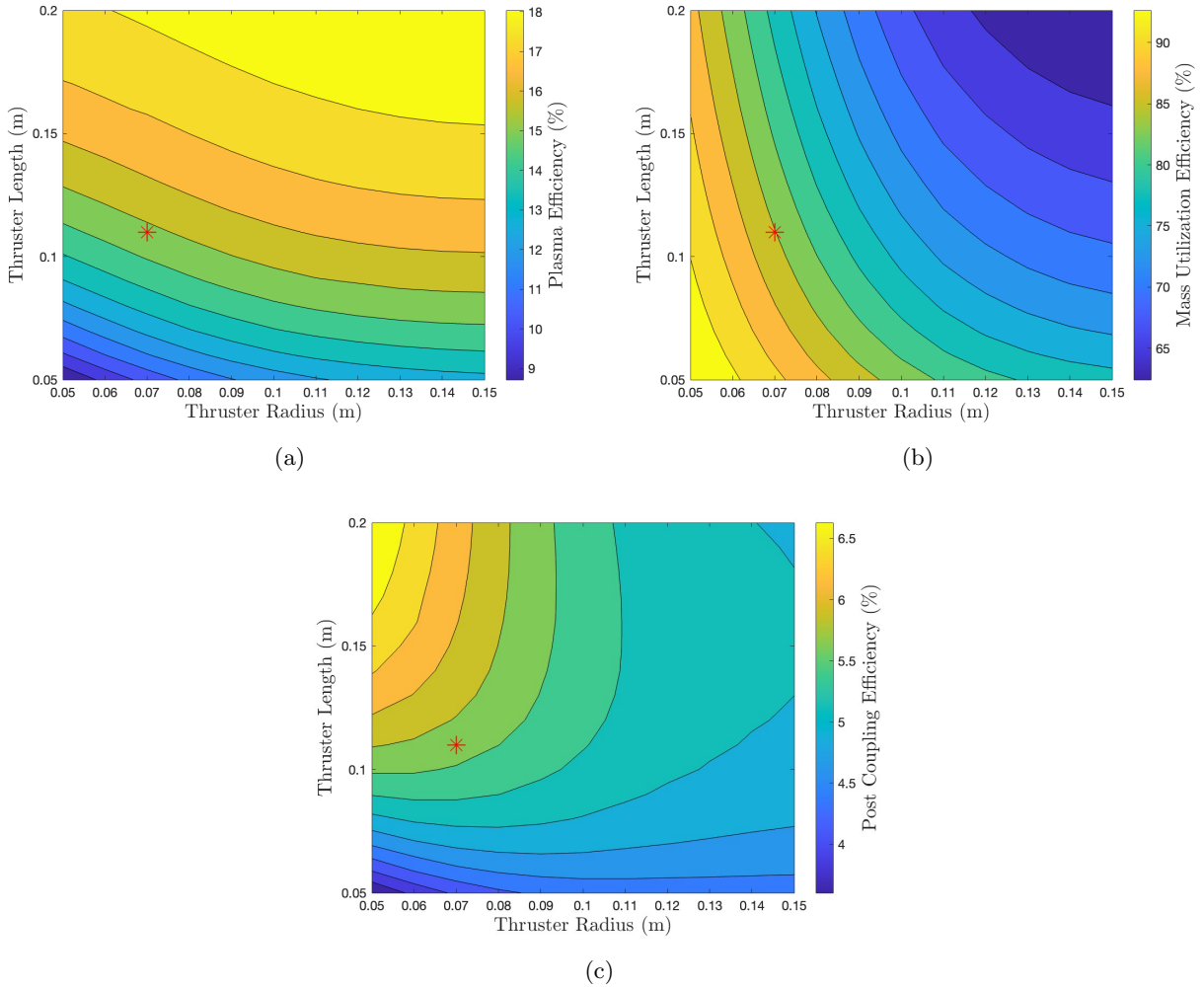

Figure 9: (a) Plasma, (b) mass utilization, and (c) post-coupling efficiency results of a trade study manipulating the thruster initial radius and length. The location of the experimental calibration data is indicated by the red asterisk marker.

3. Magnetic Field Strength Trade Study

We motivate the third trade study by considering the inter-dependence of azimuthal electron velocity (Eqn. 9) and applied magnetic field on the axial Lorentz force (Eqn. 6) dictating thrust generation. By increasing the magnitude of the RMF, with respect to the applied field, the azimuthal electron velocity will increase as electrons experience less drag forces and are able to become more closely entrained to the applied RMF frequency. However, as the axial Lorentz force is also dependent on the radial component of the applied field, it is important to maintain applied field strengths. To characterize this trend, we conducted the third trade study by varying the magnitude of the RMF and the total applied field (at a constant ratio between the radial and axial contributions) for the experimental cone angle, initial radius, and total length. To generate these results, we have assumed the experimental condition, where the radial applied field contributed 30% to the total applied field strength.

Fig 10a illustrates that as we continue to increase the field strengths, the model predicts an improvement to the plasma efficiency. Above a bias field magnitude of 150G and RMF magnitude 125G the plasma efficiency is predicted to be greater than 20%. The increase in the applied field magnitude both serves to decrease wall losses while concurrently increasing the radial field strength component necessary to boost the Lorentz force. Fig 10b, however, illustrates that at these high plasma efficiency cases, the mass utilization efficiency suffers. Again, this is a result of increased acceleration of the plasma species, in turn decreasing

the plasma density in the acceleration region of the thruster. Consequently, these lower densities lead to a reduction in ionization events, substantially driving down the mass utilization efficiency. Discussion Section D addresses this point further, and highlights that the model may be under-predicting mass utilization efficiencies. We show in Fig 10c, the post-coupling efficiency, highlighting the trade between the plasma and mass utilization efficiency. Here, we identify an optimal performance envelope in which a peak performance envelope that is achieved with lower total bias field strengths, provided an RMF magnitude of 50G is surpassed.

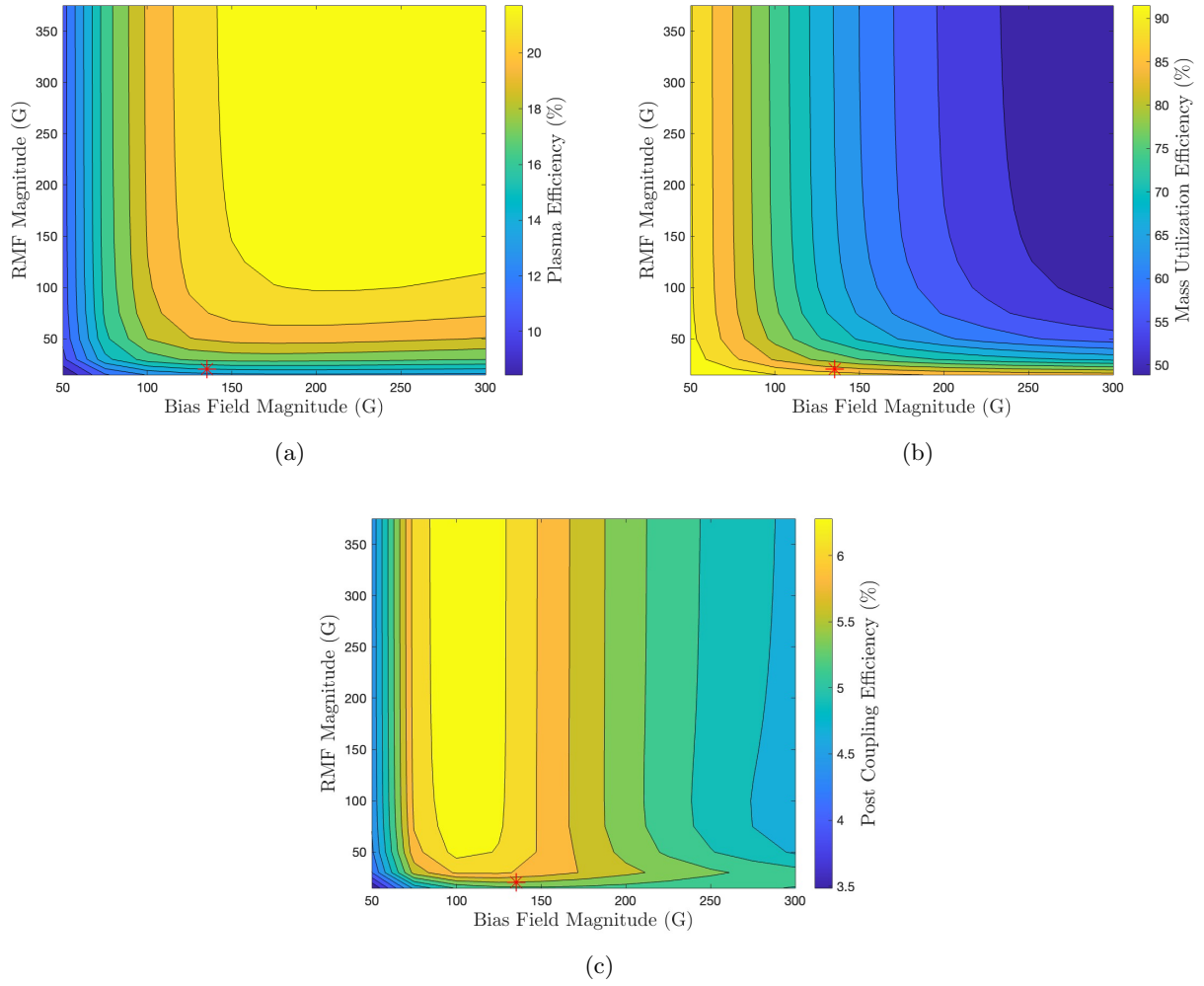

Figure 10: (a) Plasma, (b) mass utilization, and (c) post-coupling efficiency results of a trade study comparing the magnitude of the applied field to the RMF magnitude at a constant ratio between radial and axial contributions to the applied field. The location of the experimental calibration data is indicated by the red asterisk marker.

4. Trade Study Conclusions

The first design study highlighted that to increase the plasma efficiency it is vital to increase the contribution of the applied radial field strength over the axial field strength in order to generate stronger Lorentz force interactions. This in turn will increase the momentum carrying power fraction over the other power loss fractions. The second design study illuminated that increasing thruster radius and length serves to increase the plasma efficiency but commensurately decrease the mass utilization efficiency. The third design study ultimately motivated a thruster design in which the magnitude of the RMF is increased from its present value. Moreover, it underscored the necessity of maintaining an optimal ratio between the strengths of the RMF and the applied field to maximize the post-coupling efficiency.

C. Model-Driven Optimization of Design

As a last exercise, in order to evaluate the maximum possible predicted performance of the RMF thruster using this model, we seeded an unconstrained optimizer (fminsearch in MATLAB) with the experimental thurster geometry and operating conditions. We let the optimizer alter radial bias field strength, axial bias field strength, RMF strength, thruster length, thruster initial radius, and cone half-angle. The injected mass flow rate and RMF frequency were held at their experimental values.

Table 3 summarizes the initial design and the final optimized design, while Fig 11 illustrates these design changes. In addition, Table 4 summarizes the associated performance metrics and highlights the high-powered nature of an optimized RMF device, with a predicted plasma coupled power of 100kW, and an expected thrust of 1N. The results of the optimizer indicate that in order to improve post coupling efficiency, key changes must be made to improve the plasma efficiency values. Particularly, the optimizer substantially increased the magnitude of the applied radial field (seen to benefit performance in Discussion Sec. 1). This serves to increase the Lorentz force acceleration, thus leading to higher plasma velocities at the thruster exit. Commensurately, the magnitude of the applied axial field is reduced, serving to keep the overall bias field strength low as to operate in the maximum post-coupling efficiency envelope shown in Fig 10c. The magnitude of the RMF is also increased, offering better entertainment of the azimuthal electron motion to the RMF frequency, and improving the momentum carrying power, motivated via the magnetic field trade study in Discussion Sec. 3. Finally, the optimizer indicated that the idealized test article should be longer, with an smaller initial radius, at a similar cone angle to the v3 test article (consistent with results in Fig 9c). A longer thruster lengthens the acceleration region to increase the momentum carrying power. A smaller initial radius maintains high plasma densities in the ionization region of the thruster, resulting in an improved mass utilization efficiency.

As a major caveat to this study, we note that despite these improvements, the overall anticipated efficiency for the device remains comparatively low to other state of the art devices (20%). This can likely be attributed again to the the plasma efficiency. We see from the plasma power breakdown in Fig 12, that the residual thermal energy at thruster exit is the culprit for this loss process. With that said, we do not necessarily believe this is a fundamental limitation of the thruster as there are some assumptions in our model about energy transport that may be leading to overpredictions for this loss term. We elaborate on these in the following section.

Design	B_{r0}	B_{z0}	B_{ω}	Length	Radius	Cone Angle
v3 Test Article	40 G	130 G	20 G	0.1 m	0.07 m	47 deg
Optimized	106 G	32 G	290 G	0.6 m	0.03 m	38 deg

Table 3: Starting and final locations of the optimizer.

Design	η_m	η_d	η_p	η_{post}	Thrust (mN)	Plasma Power (kW)
v3 Test Article	85 %	43 %	16 %	6 %	140	6.7
Optimized	98 %	43 %	48 %	21 %	990	98

Table 4: Performance metrics associated with the starting and final locations of the optimizer.

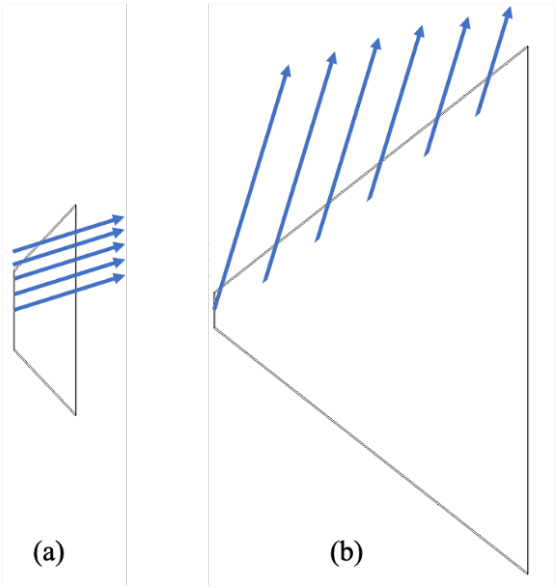

Figure 11: The geometric configuration and relative applied field contributions of (a) the v3 test article and (b) an optimized RMF thruster.

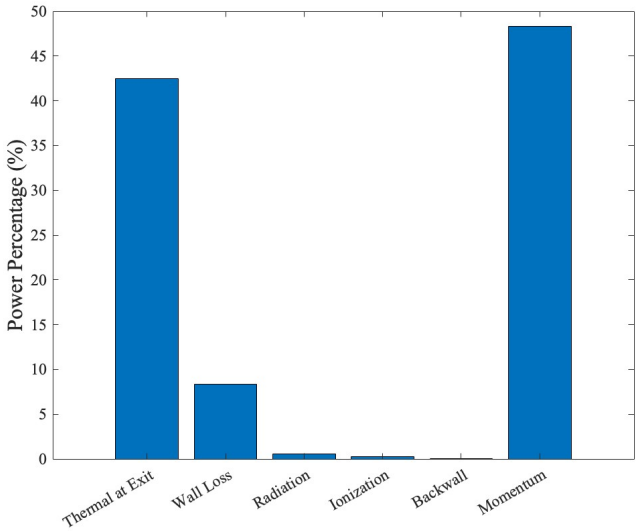

Figure 12: Plasma coupled power fractions for the optimized test article.

D. Model Limitations

As the RMF thruster is inherently a high-frequency three-dimensional device, by modeling the steady-state dynamics via a quasi one-dimensional approximation there are a number of associated model limitations. First, the divergence angle is not self-consistently calculated by the model. Instead, it is a learned constant model free parameter across all applied field magnitudes, such that the predicted divergence efficiency is constant. However, we expect the divergence efficiency to increase in the proposed optimized geometry as the decrease in cone half angle should result in a more collimated beam.

Additionally, we note the limitations of utilizing the inferred model parameters for prediction purposes. As the inferred model parameters are informed by the v3 test article, they may inherently linked to its design. With that said, as the geometries evaluated in the design trade study and optimization efforts were similar

to the v3 test article, and we expect these model parameters to hold to the proposed optimized geometry.

The last notable model limitation, a result of neglecting heat flux, drives the excessive residual thermal power losses. In reality, the applied axial magnetic fields will physically allow for heat conduction, thermalizing the electrons smoothly in the axial direction. In fact, in previous pulsed mode RMF test campaigns, triple Langmuir probe measurements indicated a peak electron temperature of ~ 10 eV.[27] However, more experimental data is needed for continuous wave operation to fully express this discrepancy. The addition of an non-zero electron heat flux will increase back plate heating as local electron temperatures will rise at the upstream boundary. However, the low mass utilization efficiencies, exhibited primarily in the third magnetic field trade study, would increase. This would result from the increase of electron temperatures at the upstream condition. In this location, where the plasma densities are the largest, an increase in electron temperature would serve to facilitate stronger ionization rates, increasing the plasma density and the overall mass utilization of the device.

VIII. Conclusion

The goal of this study was to create a one-dimensional model, including an equation for neutral continuity, ion momentum, and electron temperature, to encapsulate the physics inherent to continuous wave RMF thruster operation. Due to the low fidelity of the model, a number of coefficients were unknown which dictated the performance metrics predicted by the computational simulation. Using Bayesian inference, we tuned the free parameters by comparing the predicted performance results with the experimental measurements of both thrust and plasma coupled power. The calibrated model was able to recreate this experimental data within uncertainty bounds. We were then able to gain insight into efficiency metrics through the validated model. By further investigating the breakdown of the constituent components to the total plasma coupled power, we found that the residual thermal energy at the exit plane constituted the dominant power loss process. Results were discussed in light of model limitations primary the neglect of electron heat flux resulted in an overestimation of the electron temperatures expected within the device. Finally, to optimize thruster performance, we ran three trade studies and an global performance optimizer, to motivate the design of future RMF test articles. These trade studies demonstrated that the thruster must operate at both higher radial bias field and RMF strengths to increase the post coupling efficiency to an estimated maximum of $\sim 20\%$. However this result is likely constrained due to the assumption of a constant plume divergence angle, injected mass flow rate and RMF frequency. Overall, by creating and validating a computational framework of the RMF thruster we were able to show that there are design pathways available to improve its performance, and the technology remains a viable candidate in ongoing high power electric propulsion research.

Appendix

A. Posterior Distribution

Fig 13 shows the posterior distribution of the free parameters, specifically their 1-D and 2-D marginals. The 1-D marginals, plotted along the diagonal, indicate that the free parameters all have Gaussian distributions. However, β_m, σ, and ν_a lack tails on the left-side of their distributions due to the physical bounds set. The 2-D marginal plots, show the reliance of the free-parameters on each other. We note that the σ and ν_a free parameters are highly correlated as their sub-plot forms a linear shape. This result is expected as both parameters affect the high frequency Ohmic heating term (Eqn. 15).

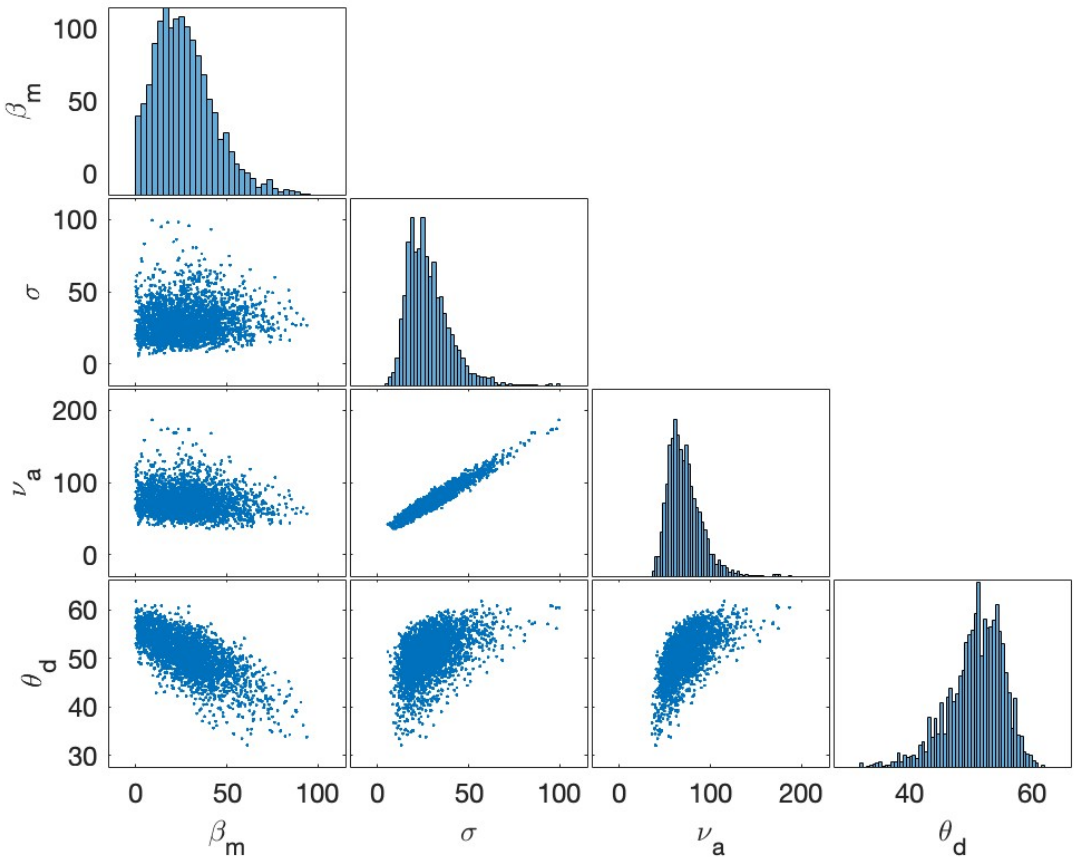

Figure 13: The 1D and 2D marginals plots of accepted model free parameters.

Acknowledgments

We would like acknowledge AFOSR Space Propulsion and Power Program for funding this work. Furthermore, the authors would like to thank Declan Brick and Dr. Thomas Marks for their guidance in our computational and modeling efforts.

References

[1] Lev, D., Myers, R. M., Lemmer, K. M., Kolbeck, J., Koizumi, H., and Polzin, K., "The Technological and Commercial Expansion of Electric Propulsion," *Acta Astronautica*, Vol. 159, 2019, pp. 213–227. https://doi.org/https://doi.org/10.1016/j.actaastro.2019.03.058, URL https://www.sciencedirect.com/science/article/pii/S0094576518319672.

[2] National Academies of Sciences, E., and Medicine, *Space Nuclear Propulsion for Human Mars Exploration*, The National Academies Press, Washington, DC, 2021. https://doi.org/10.17226/25977, URL https://nap.nationalacademies.org/catalog/25977/space-nuclear-propulsion-for-human-mars-exploration.

[3] Gallagher, H. E., "Poisoning of LaB6 Cathodes," *Journal of Applied Physics*, Vol. 40, No. 1, 1969, pp. 44–51. https://doi.org/10.1063/1.1657092, URL https://doi.org/10.1063/1.1657092.

[4] Avdienko, A., and Malev, M., "Poisoning of LaB6 cathodes," *Vacuum*, Vol. 27, No. 10, 1977, pp. 583–588. https://doi.org/https://doi.org/10.1016/S0042-207X(77)80438-7, URL https://www.sciencedirect.com/science/article/pii/S0042207X77804387.

[5] Polk, J., *The Effect of Reactive Gases on Hollow Cathode Operation*, 2006. https://doi.org/10.2514/6.2006-5153, URL https://arc.aiaa.org/doi/abs/10.2514/6.2006-5153.

[6] Goebel, D. M., and Watkins, R. M., "Compact lanthanum hexaboride hollow cathode," *Review of Scientific Instruments*, Vol. 81, No. 8, 2010, p. 083504. https://doi.org/10.1063/1.3474921, URL https://doi.org/10.1063/1.3474921.

[7] Gill, T., Sercel, C. L., Woods, J. M., and Jorns, B. A., *Experimental Characterization of Efficiency Modes in a Rotating Magnetic Field Thruster*, ???? https://doi.org/10.2514/6.2022-2191, URL https://arc.aiaa.org/doi/abs/10.2514/6.2022-2191.

[8] Polzin, K. A., "Comprehensive Review of Planar Pulsed Inductive Plasma Thruster Research and Technology," *Journal of Propulsion and Power*, Vol. 27, No. 3, 2011, pp. 513–531. https://doi.org/10.2514/1.B34188, URL https://doi.org/10.2514/1.B34188.

[9] Sercel, C. L., Gill, T. M., and Jorns, B. A., "Inductive probe measurements in a rotating magnetic field thruster," *Plasma Sources Science and Technology*, Vol. 32, No. 10, 2023, p. 105017. https://doi.org/10.1088/1361-6595/acfd5a, URL https://dx.doi.org/10.1088/1361-6595/acfd5a.

[10] Weber, T. E., "The Electrodeless Lorentz Force Thruster Experiment," Ph.D. thesis, University of Washington, 2010.

[11] Slough, J., Kirtley, D., and Weber, T., "Pulsed Plasmoid Propulsion: The ELF Thruster," *31st International Electric Propulsion Conference*, 2009.

[12] Kirtley, D., Pancotti, A., Slough, J., and Pihl, C., *Steady Operation of an FRC Thruster on Martian Atmosphere and Liquid Water Propellants*, 2012. https://doi.org/10.2514/6.2012-4071, URL https://arc.aiaa.org/doi/abs/10.2514/6.2012-4071.

[13] Furukawa, T., Takizawa, K., Yano, K., Kuwahara, D., and Shinohara, S., "Spatial measurement in rotating magnetic field plasma acceleration method by using two-dimensional scanning instrument and thrust stand," *Review of Scientific Instruments*, Vol. 89, 2018, p. 043505. https://doi.org/10.1063/1.5013214.

[14] Furukawa, T., Takizawa, K., Kuwahara, D., and Shinohara, S., "Electrodeless plasma acceleration system using rotating magnetic field method," *AIP Advances*, Vol. 7, No. 11, 2017, p. 115204. https://doi.org/10.1063/1.4998248, URL https://doi.org/10.1063/1.4998248.

[15] Gill, T. M., Sercel, C. L., and Jorns, B. A., "Experimental Investigation into Mechanisms for Energy Loss in a Rotating Magnetic Field Thruster," *37th International Electric Propulsion Conference*, 2022. URL https://pepl.engin.umich.edu/pdf/IEPC-2022-Gill.pdf.

[16] Gill, T., Sercel, C. L., Zoppi, G., and Jorns, B., "A Comparative Study of Continuous-Wave and Pulsed Operation of Rotating Magnetic Field Thrusters for Plasma Propulsion," *AIAA SCITECH 2024 Forum*, 2024. https://doi.org/10.2514/6.2024-2706, URL https://arc.aiaa.org/doi/abs/10.2514/6.2024-2706.

[17] Gill, T. M., "Fundamental Limitations of Rotating Magnetic Field Thrusters," Ph.D. thesis, University of Michigan, 2024.

[18] Takahashi, K., Charles, C., Boswell, R., and Ando, A., "Adiabatic Expansion of Electron Gas in a Magnetic Nozzle," *Phys. Rev. Lett.*, Vol. 120, 2018, p. 045001. https://doi.org/10.1103/PhysRevLett.120.045001, URL https://link.aps.org/doi/10.1103/PhysRevLett.120.045001.

[19] Goebel, D. M., and Katz, I., *Fundamentals of Electric Propulsion: Ion and Hall Thrusters*, Jet Propulsion Laboratory, 2008.

[20] Goebel, D. M., and Katz, I., *Introduction to Plasma Physics and Controlled Fusion*, 3rd ed., Springer, 2008.

[21] Sercel, C. L., "Characterization of Performance and Current Drive Mechanism for the Rotating Magnetic Field Thruster," Ph.D. thesis, University of Michigan, 2023.

[22] Hugrass, W. N., "Cylindrical plasma equilibria maintained by means of a rotating magnetic field," *Journal of Plasma Physics*, Vol. 28, No. 2, 1982, p. 369–378. https://doi.org/10.1017/S0022377800000337.

[23] Lafleur, T., Baalrud, S. D., and Chabert, P., "Theory for the anomalous electron transport in Hall effect thrusters. I. Insights from particle-in-cell simulations," *Physics of Plasmas*, Vol. 23, No. 5, 2016, p. 053502. https://doi.org/10.1063/1.4948495, URL https://doi.org/10.1063/1.4948495.

[24] Marks, T. A., and Jorns, B. A., "Challenges with the self-consistent implementation of closure models for anomalous electron transport in fluid simulations of Hall thrusters," *Plasma Sources Science and Technology*, Vol. 32, No. 4, 2023, p. 045016. https://doi.org/10.1088/1361-6595/accd18, URL https://dx.doi.org/10.1088/1361-6595/accd18.

[25] John D. Anderson, J., *Computational Fluid Dynamics: The Basics with Applications*, McGraw-Hill, Inc., 1995.

[26] Dailey, C. L., and Lovbery, R. H., "The PIT MkV Pulsed Inductive Thruster," Tech. rep., 1993. URL https://ntrs.nasa.gov/citations/19930023164.

[27] Gill, T., Sercel, C., and Jorns, B., "Experimental investigation into efficiency loss in rotating magnetic field thrusters," *Plasma Sources Science and Technology*, Vol. 33, 2024. https://doi.org/10.1088/1361-6595/ad107a.